Available online at www.sciencedirect.com
SCIENCE DIRECT®
International Journal of Multiphase Flow 32 (2006) 823–837
International Journal of Multiphase Flow
www.elsevier.com/locate/ijmulflow

Turbulent transport of particles in a straight square duct

Gaurav Sharma [a], Denis J. Phares [b,*]

[a] Department of Mechanical Engineering, Texas A&M University, College Station, TX 77843, United States
[b] Department of Aerospace and Mechanical Engineering, University of Southern California, Los Angeles, CA 90089-1453, United States

Received 22 July 2005; received in revised form 16 February 2006

Abstract

Turbulent flow through a duct of square cross-section gives rise to off-axis secondary flows, which are known to transfer momentum between fluid layers thereby flattening the velocity profile. The aim of this study is to investigate the role of the secondary flows in the transport and dispersion of particles suspended in a turbulent square duct flow. We have numerically simulated a flow through a square duct having a Reynolds number of $Re_\tau = 300$ through discretization of the Navier–Stokes equations, and followed the trajectories of a large number of passive tracers and finite-inertia particles under a one-way coupling assumption. Snapshots of particle locations and statistics of single-particle and particle pair dispersion were analyzed. It was found that lateral mixing is enhanced for passive tracers and low-inertia particles due to the lateral advective transport that is absent in straight pipe and channels flows. Higher inertia particles accumulate close to the wall, and thus tend to mix more efficiently in the streamwise direction since a large number of the particles spend more time in a region where the mean fluid velocity is small compared to the bulk. Passive tracers tend to remain within the secondary swirling flows, circulating between the core and boundary of the duct.

Keywords: Direct numerical simulation; Turbulent flow; Secondary flows; Particle transport; Inertial effects

1. Introduction

Although particle-laden turbulent flows are ubiquitous in nature and technology, a comprehensive understanding of how fine particle ensembles disperse, accumulate, and deposit has eluded researchers primarily due to the sensitivity of each particle to fine structures in the flow. Particle dynamics in a turbulent flow is therefore best studied in the Lagrangian frame of reference. Due to the practical difficulties in tracking a large number of particle trajectories over a sufficient period of time, only a few detailed experimental measurements have been reported (Virant and Dracos, 1997; Ott and Mann, 2000; La Porta et al., 2001). By contrast, time-resolved numerical simulations of Lagrangian particle motion offer fewer practical difficulties, while providing significantly larger data sets. Since definitive determination a particle's trajectory requires a detailed knowledge of the instantaneous flow structure, a direct numerical solution of the exact Navier–Stokes equations

* Corresponding author.
E-mail address: dphares@usc.edu (D.J. Phares).

0301-9322/$ - see front matter © 2006 Elsevier Ltd. All rights reserved.
doi:10.1016/j.ijmultiphaseflow.2006.02.010

offers an attractive alternative to turbulence modeling. Predictions of particle transport in most inhomogeneous flows using stochastic turbulent dispersion models intended for use with mean flow simulations lack sufficient accuracy (see discussions in MacInnes and Bracco, 1992; Yeung, 2002).

Numerous DNS studies that have enhanced our understanding of particle mixing, dispersion, and deposition have appeared in the literature. Most of these computational studies focus on homogeneous and isotropic turbulent flows in periodic domains (Yeung and Pope, 1989; Squires and Eaton, 1991; Elghobashi and Truesdell, 1992). Among those that focus on inhomogeneous turbulent flows, the circular pipe and the plane channel are the most studied wall-bounded flow geometries (McLaughlin, 1989; Brooke et al., 1994; Uijttewaal and Oliemans, 1996; Marchioli et al., 2003). Despite the currently available DNS databases, the field is still young and more simulations are needed to conclusively elucidate all the possible mechanisms by which particles disperse and deposit in inhomogeneous turbulent flows. This dictates the need for new and more detailed Lagrangian particle transport data spanning wider ranges of flow Reynolds numbers, particle Stokes numbers, and flow geometries.

This study focuses on the numerical analysis of turbulent particle transport through a duct of square cross-section. This represents a particularly interesting case of turbulent particle transport due to the inhomogeneous near-wall turbulence and the presence of turbulence-driven secondary flows. Similar flows are found in building ductwork, playing a central role in the transport of harmful air pollutants, dust, and biological aerosols from outdoor air to the indoor environment. In the present square duct flow, the directions normal to the streamwise direction are inhomogeneous and wall-bounded, unlike the widely studied plane channel flow. The two wall-bounded directions in a square duct give rise to a net secondary flow of Prandtl's second kind, which has the potential to significantly alter the turbulent particle transport compared to a plane channel. Observations of preferential concentration in a similar square duct geometry were reported by Winkler et al. (2004), who employed a large eddy simulation with particle tracking. We report new results on single-particle and pair dispersion in a duct of square cross-section using DNS coupled with Lagrangian particle tracking. The paper is organized as follows. Section 2 describes the numerical procedure for DNS and Lagrangian particle tracking. Section 3 discusses the flow simulation and presents results demonstrating agreement in computed flow statistics between the present DNS and the DNS reported by Gavrilakis (1992). The results of our subsequent computations of particle transport are presented and discussed in Section 4. Finally, Section 5 outlines conclusions drawn from the present simulations.

2. Numerical procedure

2.1. Eulerian equations of motion

The flow domain of interest is a straight square duct (Fig. 1) which is bounded by no-slip walls in the cross-stream (y- and z-) directions and the flow field is assumed to be instantaneously periodic in the statistically homogeneous streamwise (x-) direction. The governing equations of the fluid phase are the familiar Navier–Stokes equations written in their non-dimensional form as

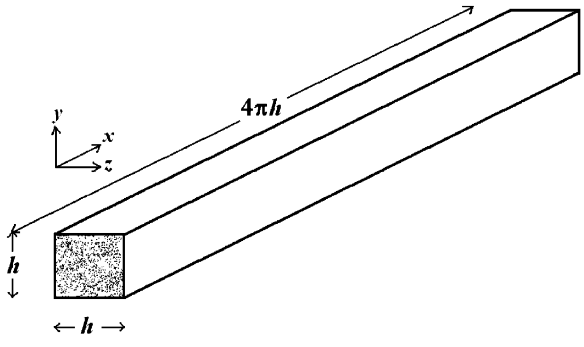

Fig. 1. Flow geometry and coordinate system for a straight square duct.

$$\nabla \cdot \boldsymbol{U} = 0, \tag{1}$$

$$\frac{\partial \boldsymbol{U}}{\partial t} + (\boldsymbol{U} \cdot \nabla)\boldsymbol{U} = -\nabla P + \Pi \hat{i} + \frac{1}{Re_\tau}\nabla^2 \boldsymbol{U}. \tag{2}$$

Here $\boldsymbol{U}(\boldsymbol{X}, t)$ is the Eulerian flow velocity given by $\boldsymbol{U}(\boldsymbol{X}, t) = (u, v, w)$ at a fixed point in space, $\boldsymbol{X} = (x, y, z)$, and at time t. The characteristic scales of duct flow used for non-dimensionalization of these equations are the duct hydraulic diameter, h, and mean friction velocity, u_τ^a. The mean friction velocity here is known a priori from the imposed static pressure gradient, Π, used to derive the bulk flow in the homogeneous streamwise direction ($\hat{i}$ is the unit vector along x-direction). The imposed static pressure gradient is used to calculate the mean friction velocity for non-dimensionalization, even though the actual four-wall, spatial-averaged friction velocity will slightly fluctuate in time about this mean value. The friction Reynolds number is defined as $Re_\tau = hu_\tau^a/\nu = 300$, where ν is the kinematic viscosity of the Newtonian fluid. The present value of $Re_\tau = 300$ corresponds to a bulk Reynolds number, $Re_b \sim 4410$, and a centerline Reynolds number, $Re_c \sim 5880$ (Gavrilakis, 1992). The dimensions of the square duct are $4\pi h \times h \times h$ (see Fig. 1). In terms of wall units, the dimensions of the duct are $L_x^+ = 3770$ and $L_y^+ = L_z^+ = 300$. The present streamwise length of $L_x^+ = 3770$ wall units is sufficiently long to accommodate the streamwise-elongated near-wall structures present in wall-bounded shear flows. These near-wall structures are rarely expected to be longer than about 1000 wall units in the streamwise direction (Robinson, 1991). A uniform Cartesian grid of $327 \times 195 \times 195$ is used, totaling 12.43 million computational grid points. The grid resolution is $\Delta x^+ = 11.67$ wall units in the streamwise direction and $\Delta y^+ = \Delta z^+ = 1.57$ wall units in the wall-normal directions. The first grid point away from the wall is located at $\Delta y^+/2 = \Delta z^+/2 = 0.79$ wall units, due to a staggered grid. The Kolmogorov length scale for this flow based on the volume-averaged dissipation is estimated to be little over 2 wall units (Gavrilakis, 1992). The present grid is therefore sufficient for resolving all of the dynamically significant length scales of interest without requiring sub-grid scale modeling. We have used a uniform grid, rather than a stretched grid, in order to maintain the small Δy^+ and Δz^+ values in the interior of the flow domain necessary for accurate particle tracking throughout the duct. The small fixed time step for time integration was $\Delta t = 1.5\text{e}{-4}$ or equivalently $\Delta t^+ = 4.5\text{e}{-2}$ time wall units, corresponding to a time-mean CFL value of 0.28 in the present flow simulation.

The spatial derivatives in the equations above are discretized on a Cartesian staggered mesh. The inertial and viscous terms in the momentum equations are approximated in the interior of the flow domain by fourth-order accurate central differences, and all other spatial derivatives in the Eulerian equations of motion are at least second-order accurate. Near the boundaries, all derivatives are second-order accurate with the exception of inertial terms for which a third-order accurate upwind-biased formula is used. The pressure Poisson equation is solved using a fast Poisson solver algorithm. The momentum equations are integrated in time using an explicit, second-order accurate Adams–Bashforth method.

2.2. Lagrangian equations of motion

We consider particles with inertia and passive tracers, point-like (imaginary) particles with vanishing inertia with respect to the advecting fluid. The particle equations of motion given here are also non-dimensionalized by the duct hydraulic diameter (h) and mean friction velocity (u_τ^a). The Lagrangian and Eulerian fluid velocities are related for a passive tracer particle by

$$\frac{\mathrm{d}\boldsymbol{X}_p}{\mathrm{d}t} = \boldsymbol{U}_p(t) = \boldsymbol{U}(\boldsymbol{X}, t), \tag{3}$$

where $\boldsymbol{X}_p(t)$ is the particle position at time t, $\boldsymbol{U}_p(t)$ is the Lagrangian velocity of a particle at time t. The instantaneous location of a particle at time t is given by $\boldsymbol{X}_p(t)$ and the instantaneous particle velocity at this moving point is $\boldsymbol{U}_p(t)$.

The Lagrangian motion of a rigid, spherical particle suspended in a flow is governed by a force balance equation that is described in detail by Maxey (1987). Even though a number of possible forces (including Stokes drag, lift, gravity, virtual mass, and Basset history) can act on a finite-inertia particle, many of these may be neglected without any appreciable loss of accuracy, depending on the particle inertia. The most

important force acting on the particle is the Stokes drag force. Gravity may be another important force to include depending on the geometrical orientation of the flow of interest. In this study, we neglect gravity in order to resolve the effect of the secondary flows. We also neglect the shear-induced Saffman lift force (Saffman, 1965) because it only assumes non-trivial magnitudes in the viscous sublayer. Even in the viscous sublayer, it has been found to be an order of magnitude smaller than the normal component of the Stokes drag force (McLaughlin, 1989). Particle deposition data obtained by DNS computations of McLaughlin (1989) and others have revealed that, depending on the particle inertia, there is only a small difference in the statistical results from simulations performed with and without consideration of the lift force. Furthermore, the Saffman lift force becomes less important for particles with large particle–fluid density ratios or large response times. Therefore, we consider the Stokes drag as the only significant force acting on a finite-inertia particle. As a further simplification we have assumed one-way fluid–particle coupling so that the particles are affected by the fluid motion but not vice-versa. This assumption is reasonable if the suspended particles are small in size compared to the Kolmogorov length scale (η) of flow and for the case of low-mass loading.

The finite-inertia particles are assumed to be rigid, spherical and to have a density much higher than that of the fluid (i.e. $\rho_p/\rho_f \gg 1$), in order for the assumption of point forces to be valid. With all of the above assumptions, the non-dimensional force balance equation takes the form

$$\frac{d\boldsymbol{U}_p}{dt} = \frac{\boldsymbol{U} - \boldsymbol{U}_p}{\tau_p}. \tag{4}$$

The term on the right hand side represents the effect of the linear Stokes drag force. The dimensionless particle response time, τ_p, is a measure of the relative importance of particle inertia and fluid acceleration and is defined here as

$$\tau_p = \frac{\rho d_p^2 Re_\tau}{18}, \tag{5}$$

where ρ is the particle–fluid density ratio ($\rho = \rho_p/\rho_f$) and d_p is the dimensionless particle diameter. In the present non-dimensionalization, the dimensionless particle relaxation time is equal to the commonly used Stokes number, and it completely determines the particle dynamics in a specified flow field. We use a range of τ_p^+ values between 0 and 300, where $\tau_p^+ = \tau_p Re_\tau$ and $\tau_p^+ = 0$ corresponds to a passive tracer. The density ratio for the finite-inertia particles is chosen to be $\rho = 763$, which corresponds to olive oil droplets in air at 25 °C, or $\rho = 2083$ (glass microspheres). For a chosen value of τ_p^+, the density ratio determines the particle diameter. In the present simulations, the selected density ratios yield particle diameters that are smaller than the estimated Kolmogorov length scale for this flow.

The governing equations of particle motion are integrated using a fourth-order accurate Runge–Kutta method and a small fixed time step equal to the Eulerian flow advancement time step. In a study focusing on the performance of three interpolation schemes (trilinear, bicubic splines and tricubic interpolation) for particle tracking, Rovelstad et al. (1994) found tricubic interpolation particularly attractive since it provides high accuracy, fast computation and continuous first-order derivatives of interpolated velocities. Therefore, Eulerian fluid velocities at intermediate points in the computational domain are determined using a tricubic interpolation scheme. We use periodicity in the streamwise direction for particles as well, allowing particle tracking over larger displacements in the x-direction. A particle is considered to deposit when it reaches a distance from the wall that is equal to or less than its radius determined by Eq. (5).

3. Flow simulation and validation

The low Reynolds number turbulent flow was simulated starting from perturbed laminar flow initial conditions. The laminar flow was perturbed using random numbers in $[-1, 1]$ with small initial perturbation amplitudes of 10^{-6}. The perturbed flow field was allowed to evolve until a fully developed and statistically stationary turbulent flow state was reached, at which point the time was explicitly reset to zero. This state was used as the fully developed turbulent flow initial condition for subsequent flow averaging and particle transport computations. The two-point streamwise velocity cross-correlation coefficients were found to decay significantly over a streamwise length of $L_x/2$, thus demonstrating the adequacy of the simulation duct length

and suggesting that the duct length can accommodate the streamwise-elongated structures present in this turbulent flow.

We have verified our numerical procedure through comparisons with the DNS results on a similar geometry presented by Gavrilakis. These comparisons are presented in Figs. 2 and 3 and Table 1, where the y/h (or z/h)

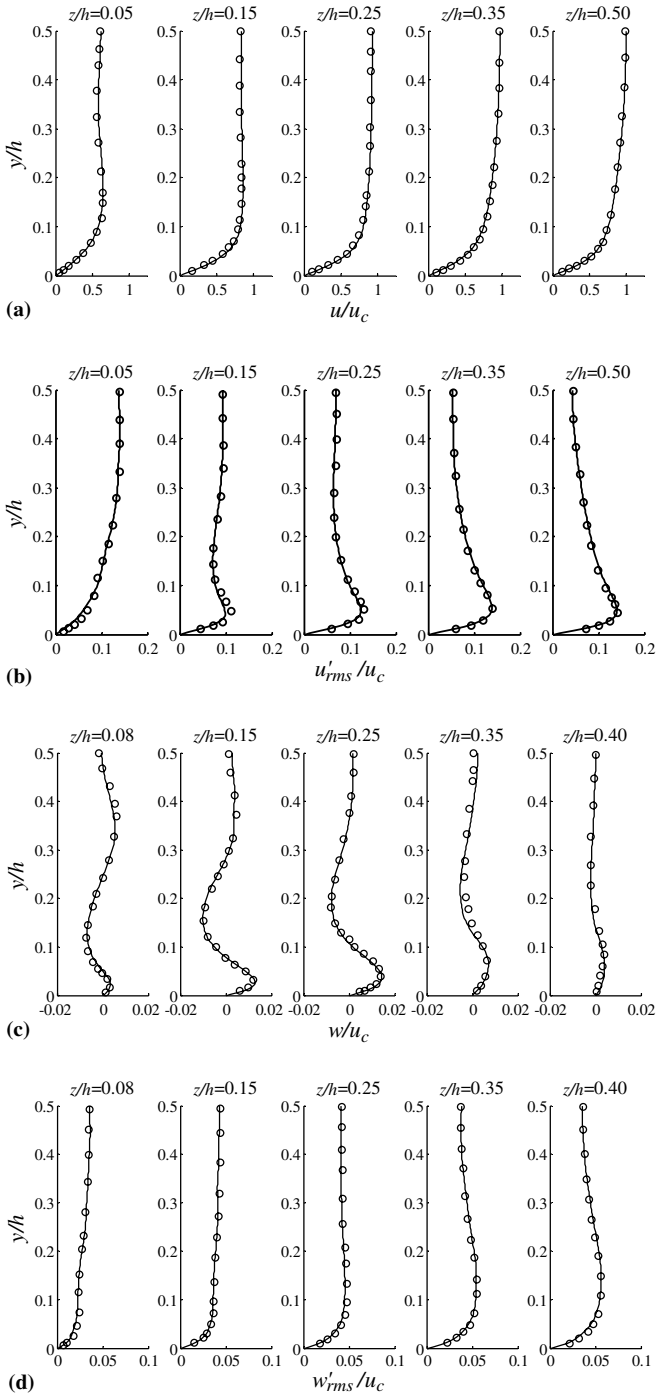

Fig. 2. Quadrant-averaged profiles at five locations in the duct for: (a) the mean streamwise velocity, (b) rms fluctuations in streamwise velocity, (c) mean lateral velocity and (d) rms fluctuations in lateral velocity. (a–d) (—) Present DNS (○), Gavrilakis.

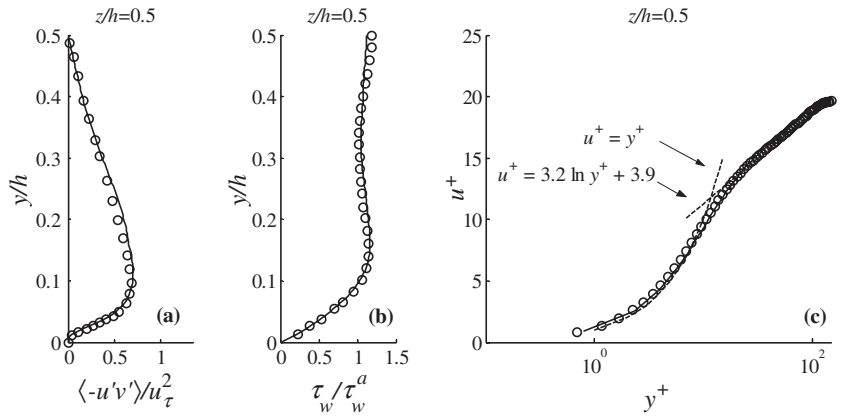

Fig. 3. (a) Quadrant-averaged profile of the primary Reynolds stress component, $\langle -u'v' \rangle$, normalized by local wall-friction velocity at mid-wall location. (b) Profile of wall shear stress as a function of distance along the wall and normalized by the average shear stress over the wetted area of duct. (c) Profile of mean streamwise velocity component at duct centerline on a log-linear scale and normalized by the mean friction velocity. Shown also is the corresponding profile from Gavrilakis DNS and profiles of the law of the wall and the log-law. (a–c) (—) Present DNS (○), Gavrilakis.

Table 1
Comparison of flow quantities computed in present DNS and their corresponding values computed by Gavrilakis and Vazquez & Metais

Computed flow quantity	Present DNS ($Re_\tau = 300$)	Gavrilakis DNS ($Re_\tau = 300$)	Vazquez and Metais LES ($Re_\tau = 393$)
u_c/u_b	1.32	1.33	1.29
$\tau_{w\|0.5}/\tau_w^a$	1.12	1.18	1.11
$u_{\tau\|0.5}/u_\tau^a$	1.06	1.09	1.05
F_f	0.035	0.037	–
u_τ^a/u_b	0.0663	0.0680	0.0655

label represents the distance from the wall. In Figs. 2 and 3, the solid lines represent the present DNS data while the circles represent data from the DNS simulation of Gavrilakis.

The flow statistics were obtained over a period of about eight non-dimensional time units. Geometrical (and flow) symmetry and homogeneity along the x-direction were exploited while computing the quadrant-averaged data. Fig. 2(a) and (b) display the quadrant-averaged profiles of the mean and fluctuating streamwise velocity components, respectively, at five locations of the square duct. Fig. 2(c) and (d) display the mean and fluctuating lateral velocity components at five locations. All of the velocity profiles in Fig. 2(a)–(d) are normalized by the mean value of the streamwise velocity at the duct centerline, u_c. Fig. 3(a) shows the quadrant-averaged primary component of the Reynolds stress at the duct centerline. The Reynolds stress is normalized by the square of the mid-wall friction velocity computed in the simulation ($u_{\tau|0.5}$). Fig. 3(b) shows the computed wall shear stress profile as a function of distance along the wall. The wall shear stress is normalized by the average shear stress over the wetted area of the duct (τ_w^a). Note that the values of τ_w^a and u_τ^a are known from the imposed uniform pressure gradient and are both equal to unity in the present non-dimensionalization. Fig. 3(c) shows the mean streamwise velocity profile on a log-linear scale along with the velocity profiles reported by Gavrilakis, the law of the wall and log-law profiles. Table 1 lists the numerical values of some other computed flow quantities along with their corresponding values from the Gavrilakis DNS study and the isothermal LES study of Vazquez and Metais (2002). The listed flow quantities are the ratio of computed mean centerline velocity to the average bulk velocity (u_c/u_b), ratios of the computed mid-wall shear stress to the four-wall-averaged shear stress ($\tau_{w|0.5}/\tau_w^a$) and the ratio of their corresponding friction velocities ($u_{\tau|0.5}/u_\tau^a$), computed friction factor ($F_f = 8(u_\tau^a)^2/u_b^2$) and the ratio of mean friction velocity to the computed bulk velocity (u_τ^a/u_b). It is clear from the figures and Table 1 that there is a generally good agreement between the present DNS and the DNS presented by Gavrilakis, indicating that our methodology and flow resolution are sufficient.

4. Particle transport results and discussion

We have obtained Lagrangian statistics of passive tracers and finite-inertia particles from two different problem formulations (Cases A and B). Case A features the release of 25,600 uniformly distributed particles in a plane at the duct inlet, and Case B features the release of 24,892 particle pairs uniformly distributed in the core of the duct. In each case, all particles are smaller than the estimated Kolmogorov length scale of 2 wall units.

4.1. Visualization of preferential concentration

In inhomogeneous wall-bounded turbulence, preferential concentration of particles is characterized and enhanced by the near-wall coherent motions of the turbulent boundary layer. In a recent study, Winkler et al. (2004) studied the preferential concentration of particles in a square duct flow using LES at $Re_\tau = 360$. The authors of that study observed that finite-inertia particles tend to accumulate in regions of high strain rate and empty regions of high vorticity, as previously noted by Maxey (1987). However, particles were found to accumulate close to the wall despite high magnitudes of vorticity. In the present study, particle accumulation patterns are visualized on two different planes. Figs. 4 and 5 show snapshots of the dispersed particles for $\tau_p^+ = 15$ (Fig. 4(a)–(d)) and $\tau_p^+ = 0$ (Fig. 5(a)–(c)) after an initial release of 64,000 uniformly distributed particles in planes located within the viscous sublayer ($y_0^+ = 3$) above the duct walls. Fig. 4 shows the particle locations in an x–z-plane and a y bin of width 30 wall units ($0 \leqslant y^+ \leqslant 30$), corresponding to a top view of the bottom wall. Starting from an initially uniform distribution (Fig. 4(a)), the early evolution of the particle distribution exhibits patterns characteristic of flow structures present in a turbulent boundary layer (Fig. 4(b) and (c)). The late time particle distribution exhibits particle accumulation near the streamwise-elongated streaks (Fig. 4(d)). In the near-wall region, the motion of advecting vortices near the streamwise-elongated streaks is largely responsible for bringing particles closer to the low-velocity streaks. Fig. 5(a)–(c) exhibit passive tracer locations in a y–z-plane (located at $x = L_x/2$). At early times, the particles released near the wall are carried into the duct interior by corner vortices present due to turbulence-driven secondary flow. This

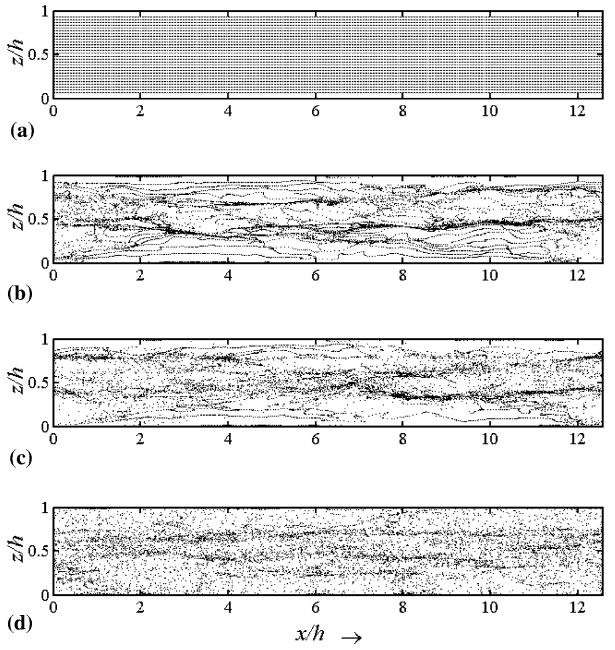

Fig. 4. Instantaneous particle positions for $\tau_p^+ = 15$ particles at $t^+ =$ (a) 0, (b) 135, (c) 270 and (d) 675 for an initial release height of $y_0^+ = 3$. Particles are visualized in the x–z-plane and a y bin of width 30 wall units from the bottom wall.

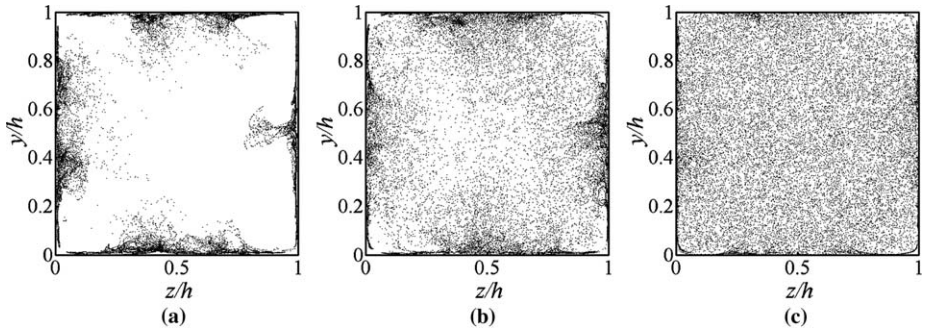

Fig. 5. Instantaneous particle positions for passive tracer particles at $t^+ =$ (a) 135, (b) 270 and (c) 675 for an initial release height of $y_0^+ = 3$. Particles are visualized in the y–z-plane and a x bin that is 150 wall units wide ($h/4$ wide on either side of $x = L_x/2$).

transport mechanism is unique to the present square duct geometry, as opposed to a circular pipe or a plane channel. At a later time ($t^+ = 675$ in Fig. 5(c)), the passive tracers are distributed throughout the entire domain with a nearly homogeneous distribution in the core of the duct.

4.2. Single-particle dispersion

4.2.1. Longitudinal dispersion

Fig. 6 displays the mean square x-displacement of an ensemble of passive tracers from the Case A simulation. The displacements are calculated relative to the average fluid x-velocity in the duct, $u_b = 15.69$, as calculated from the flow simulation. The initial t^2 dependence is expected, as the particles are carried away from the mean fluid flow by advection. For example, the displacement of the ith particle relative to the mean flow may be written

$$x_i - u_b t = (\Delta u_i + u_i')t, \tag{6}$$

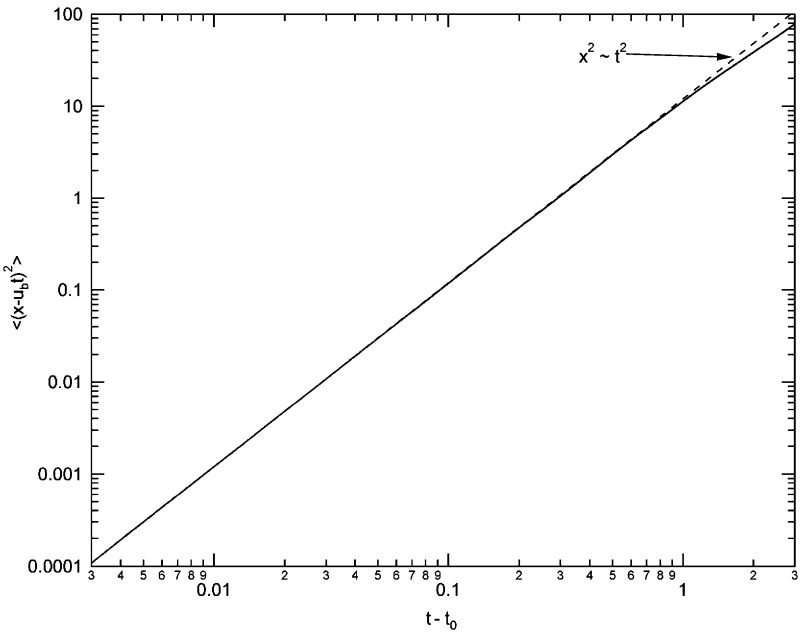

Fig. 6. Mean square longitudinal displacement (relative to bulk flow) of passive tracers versus time.

where Δu_i is the difference between the local mean fluid x-velocity and the mean fluid x-velocity averaged over the duct cross-section (u_b), and u_i' is the local instantaneous deviation from the mean. After roughly 1 dimensionless time unit, the mean square x-displacement has a sub-linear dependence on time. For a circular pipe, the particle transport would eventually approach a Taylor regime, characterized by a uniform particle distribution throughout the pipe cross-section and a symmetric distribution in the longitudinal direction. In this regime, the mean square relative displacement would be proportional to t, indicative of a diffusion process. This so-called Taylor dispersion arises because the longitudinal advection of particles through a fluid cell moving at the average fluid velocity is balanced by the lateral diffusion of particles through the fluid cell. This mass balance may be expressed in two dimensions as

$$E(y)\frac{\partial^2 C'}{\partial y^2} = \Delta u \frac{\partial \overline{C}}{\partial \xi}, \tag{7}$$

where $E(y)$ is the lateral mixing coefficient, $\overline{C}$ is the particle concentration averaged over the pipe cross-section, C' is the local deviation from the mean concentration, and $\xi = x - u_b t$. The solution of Eq. (7) reveals that the mass flux in the longitudinal direction is proportional the streamwise concentration gradient. It is this fortuitous result that allowed Taylor to treat the longitudinal motion of a passive tracer as a diffusion process (Taylor, 1954).

Although the deviation from the initial $x \sim t$ behavior in Fig. 6 likely corresponds to a transition regime prior to an analogous Taylor-like regime for the square duct, we stipulate that a Taylor-like regime does not exist, because the lateral motion of the particles is driven by both turbulent diffusion and advection by off-axis secondary flows. Thus, the analogous mass balance expression must be written:

$$E(y)\frac{\partial^2 C'}{\partial y^2} - v(y)\frac{\partial C'}{\partial y} = \Delta u \frac{\partial \overline{C}}{\partial \xi}. \tag{8}$$

The additional term in Eq. (8) ensures that the resulting mass flux is not proportional to the streamwise concentration gradient, preventing the onset of a Taylor-like regime for long simulation times. Therefore, the plot of $\langle (x - u_b t)^2 \rangle$ versus time in Fig. 6 is not expected to ever exhibit the linear dependence observed for passive tracers in pipes or channels.

Unlike passive tracers, the dispersion of finite-inertia particles is sensitive to the initial velocity condition until at least several particle relaxation times from their release. Consequently, it makes sense to normalize the displacement and time with τ_p, as shown in Fig. 7. With this scaling, the data initially collapse to a single curve. Since the particles in the Case A simulations were released from rest, the initial trajectory of a particle may be derived from Eq. (3):

$$\frac{x_p}{\tau_p} = u\left(\frac{t}{\tau_p} - 1 + e^{-\frac{t}{\tau_p}}\right), \tag{9}$$

yielding

$$\frac{\left(\langle (x_p - u_b t)^2 \rangle\right)^{1/2}}{\tau_p} = \left((\langle u^2 \rangle)\left(\frac{t}{\tau_p} - 1 + e^{-\frac{t}{\tau_p}}\right)^2 + \left(u_b \frac{t}{\tau_p}\right)^2 - 2u_b \langle u \rangle \frac{t}{\tau_p}\left(\frac{t}{\tau_p} - 1 + e^{-\frac{t}{\tau_p}}\right)\right)^{1/2}. \tag{10}$$

Eq. (10) is plotted in Fig. 7, using $u_b = 15.69$, $\langle u \rangle = 17.87$, and $\langle u^2 \rangle = 333.7$. These values represent the best fit through the data. Note that the velocity, u_b, of the fluid averaged over the entire duct cross-section is less than the average velocity, $\langle u \rangle$, of the ensemble of particles, which initially are not present very close to the duct walls where the fluid velocity is small.

As the curves begin to deviate from Eq. (10), the effect of inertia becomes evident, as high inertia particles actually appear to disperse more quickly from the mean fluid flow than low-inertia particles. In fact, the curves quickly attain limiting power law behaviors within the simulation time, and the exponent increases with relaxation time. When the best fit value for the exponent is plotted against the particle relaxation time, as displayed in Fig. 8, a monotonically increasing function is revealed, where the exponent varies between 1 and 2.

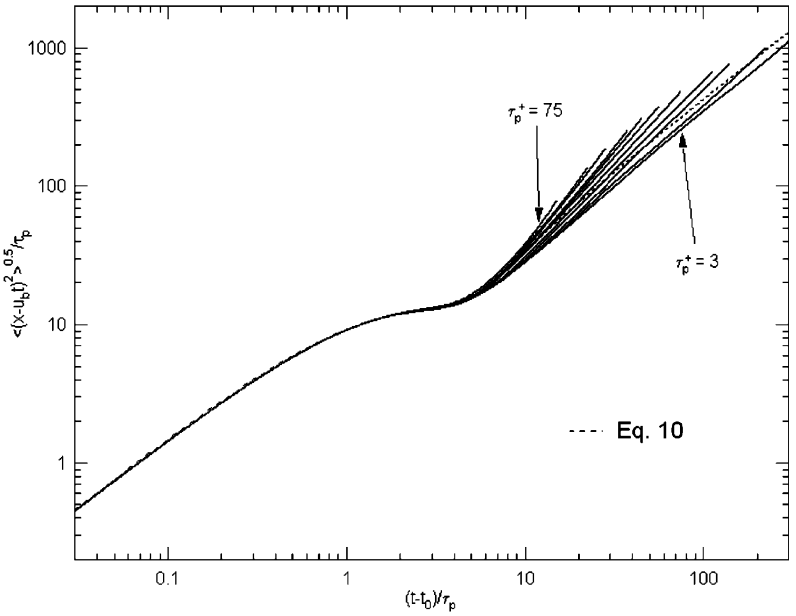

Fig. 7. Normalized longitudinal displacement of finite-inertia particles versus time ($\tau_p^+ = 3, 5, 8, 10, 15, 20, 25, 30, 40, 50, 75$).

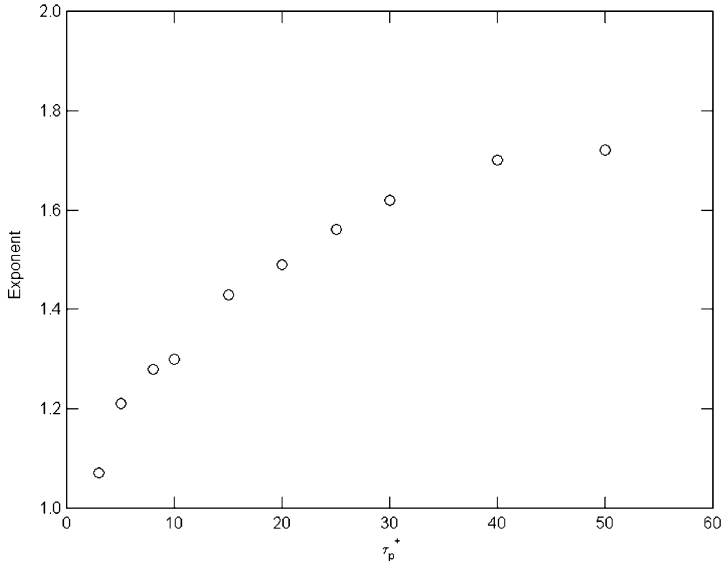

Fig. 8. Exponent from apparent power law relation between displacement and time versus dimensionless particle response time.

Although we will stop short of discussing why a power law relation may exist for finite-inertia particles, we can explain the general trend through direct visualization of the particles. Firstly, we note that the trend is not an artifact of the enhanced deposition of the higher inertia particles, because deposited particles were immediately removed from the averaging process. Rather, the ensemble of higher inertia particles is smeared in the streamwise direction more rapidly than the lower inertia particles because they tend to accumulate within the boundary layer and thus spend more time traveling at a much lower velocity than the mean fluid velocity. This is evidenced in Fig. 9, which displays snapshots of the particles in the xy-plane for (a) $\tau_p^+ = 0$ and (b) $\tau_p^+ = 30$ at an early time (grey) and a late time (black) in the simulation. Note that the concentration profiles are indeed

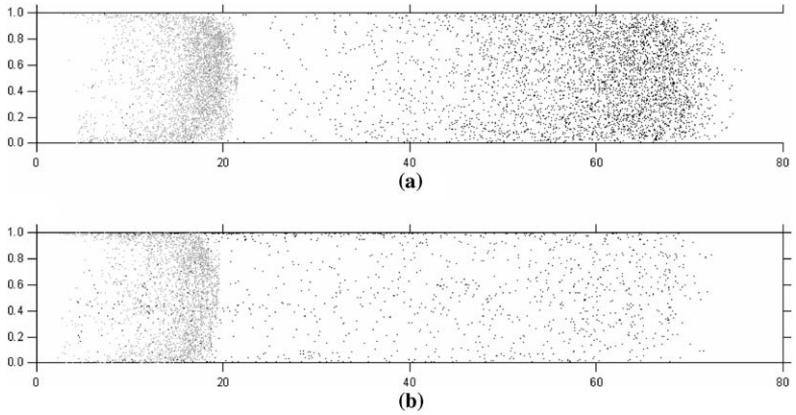

Fig. 9. Snapshots of particle locations in xy-plane for (a) passive tracers and (b) $\tau_p^+ = 30$. The grey dots correspond to an early time and the black dots correspond to a later time.

asymmetric in the streamwise direction for both cases, but that the tail of the distribution is more predominant for the high inertia particles, primarily because a larger fraction of them are close to the walls.

4.2.2. Lateral dispersion

The longitudinal dispersion of particles is inherently linked to their lateral motion, which transfers them between fluid cells having varying mean x-velocities. The relatively complex lateral motion of particles in a square duct consisting of both advection and diffusion warrants further scrutiny.

Fig. 10 displays results from Case A, where particles are released uniformly in the yz-plane, again neglecting particles that have deposited to the duct walls. The coordinate $r = (y^2 + z^2)^{1/2}$ is used to denote distance traveled normal to the streamwise direction. Fig. 10 is analogous to the plot presented by Uijttewaal and Oliemans (1996) for turbulent transport in a circular pipe (Fig. 13, in that study). The authors of that study note that when they plot $\langle (r - r_0)^2 \rangle$ versus t^+ for various values of particle inertia, all of the curves initially exhibit a t^2

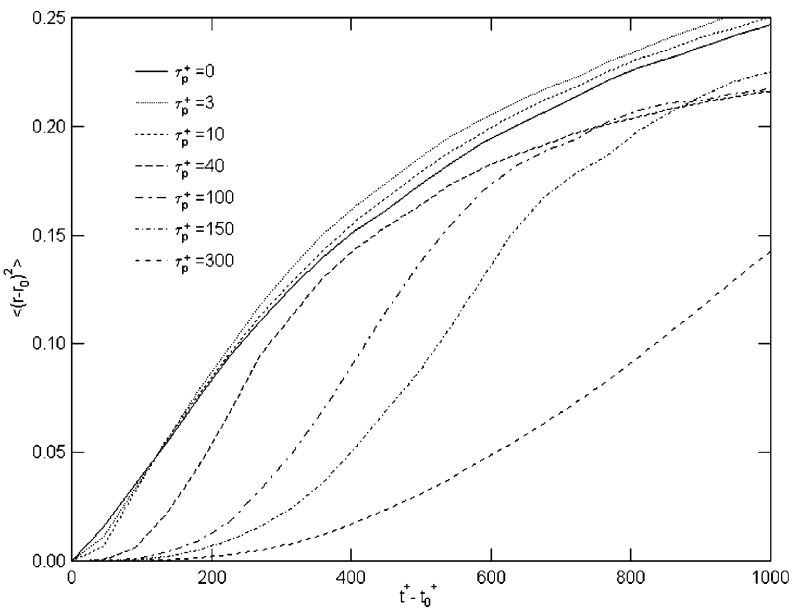

Fig. 10. Mean square lateral displacement versus time.

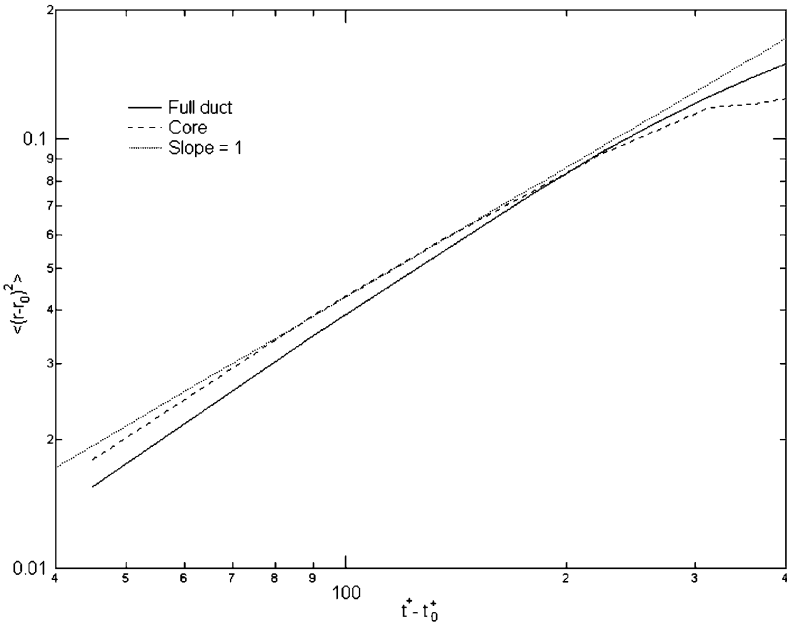

Fig. 11. Comparison of mean square lateral displacement of passive tracers between those located in the entire duct and those confined to the core of the duct. The slope = 1 line corresponds to purely diffusive transport.

dependence, and then become linear with time, indicative of a diffusion process. They exploit the linear part of the curves to calculate a lateral dispersion coefficient, D:

$$D = \frac{1}{2}\frac{\mathrm{d}\langle (r - r_0)^2 \rangle}{\mathrm{d}t} \tag{11}$$

and present the results as a function of particle inertia.

By contrast, no obvious linearity exists in Fig. 10, indicating that turbulent diffusion is not the sole means of lateral transport and further underscoring the lack of a Taylor regime for the *longitudinal* dispersion of particles in a square duct. This is especially evident from Fig. 11, which displays the passive tracer result on a log–log scale. Since Uijttewaal and Oliemans (1996) confined their dispersion calculations to particles located within $0.354D$ of the pipe centerline, we have included a similar calculation in Fig. 11. Note that there exists a super-linear relation between the mean square lateral displacement and time indicative of the advective lateral transport, but that the slope approaches unity when only core particles are considered. This is consistent with a situation where the secondary flows become more important to the lateral transport of particles farther away from the duct centerline.

Fig. 12 displays the data normalized by τ_p, the same scaling used in Fig. 7, and plotted on a log–log scale along with the expected slope line for transport by turbulent diffusion. It is clear from the plot that lateral transport and mixing is more efficient for low-inertia particles, when normalized by the particle relaxation time. This is the opposite trend from that evident in Fig. 7, where longitudinal mixing is seen to occur more efficiently for higher inertia particles. This is not too surprising since longitudinal dispersion is enhanced if particles are not efficiently transported laterally between fluid layers.

4.3. Pair dispersion

The relative dispersion of particle pairs is commonly computed in unconfined flows to study the relative importance of different eddy length scales to the dispersion of suspended particles. Consequently, the concept of relative dispersion in an internal flow is not as meaningful since the eddy length scales are limited. However, in light of the fact that the relatively well-defined larger-scale secondary flow eddies appear to have an

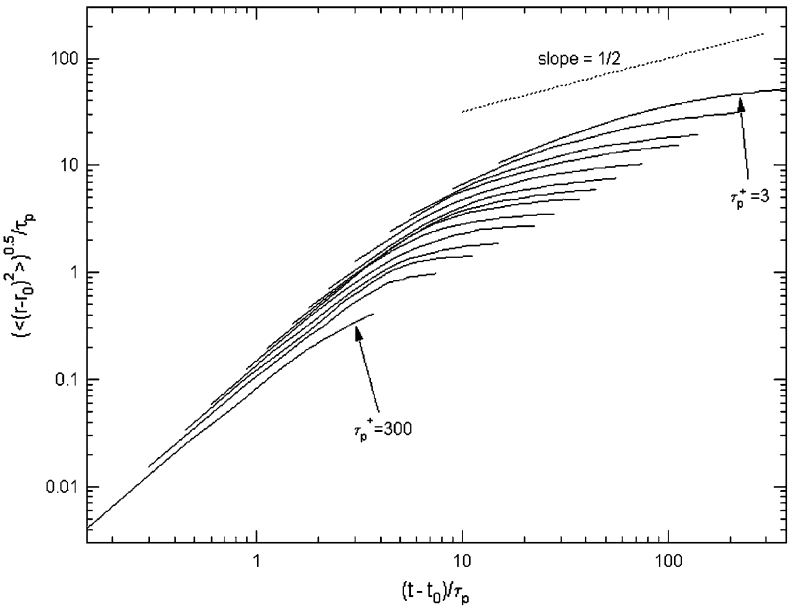

Fig. 12. Normalized lateral displacement of finite-inertia particles versus time ($\tau_p^+ = 3, 5, 8, 10, 15, 20, 25, 30, 40, 50, 75, 100, 150, 300$).

influence on the dispersion of particles in a square duct, we have computed the mean square lateral separation of particle pairs. Again, any particle that deposited on the duct walls was not counted in the averaging process. In each of these simulations, 24,892 particle pairs were released uniformly in the core of the duct ($y^+ > 100$) in a three-dimensional box, whose size was dependent on the initial separation of the particles. As the simulation progresses, it is expected that the separation will initially depend on the local small-scale structure of the turbulence, and eventually the effect of the secondary flows will become evident when the separation of the particle pairs is similar to the size of the secondary flow eddies.

The computational results are presented in Fig. 13 for $\tau_p^+ = 0, 5, 15$, and 30 and for initial particle separation of $r_0^+ = 0.5, 2, 8, 16, 20, 24$. The Kolmogorov length scale for this flow is roughly $\eta^+ = 2$ (Gavrilakis, 1992), so the selected initial separations range from 0.25 η^+ to 12 η^+. The data represent two-dimensional separations in the yz-plane, where $\langle \Delta^2 \rangle = \langle (y_1 - y_2)^2 + (z_1 - z_2)^2 \rangle$. Up to 1 dimensionless time unit, the mean square separations exhibit power laws with an exponent that decreases with r_0^+. These indicate similarity of the local small-scale turbulence. For larger initial separations ($r_0^+ > 2$), all of the curves remain collapsed until $t = 1$, beyond which the curve corresponding to passive tracers quickly levels off, deviating from the curves corresponding to the finite-inertia particles. This consistently occurs at a mean square separation of $\langle \Delta^2 \rangle \sim 0.17$. This value is comparable to the square of the size of the mean secondary swirling flows, which may be estimated from Fig. 2(c). That figure, which displays the mean off-axis velocity as a function of distance from the wall, reveals that the secondary flows extend from close to the duct wall to a distance of between 0.3 and 0.4 into the duct core. Thus, when the mean square separation of particle pairs in the duct approaches the square of the size of the secondary flow eddies (between 0.1 and 0.2), an inertia-dependent response is expected. Physically, it appears that the passive tracer pairs tend to follow the mean off-axis flow, becoming trapped in the mean circulation and thus quickly attaining a limiting mean separation. By contrast, particles with finite-inertia are more likely to be thrown out of the mean swirl after a finite period of time. It is unlikely that centrifuging initiated by the mean swirl is responsible for this inertia-dependent effect, because the appropriate Stokes number based on the size of the recirculation flow and the mean off-axis velocity is much smaller than unity for all of the particle sizes considered. However, the inertia-dependent separation of particles from the mean recirculation may be caused by turbophoresis (Reeks, 1977). Finite-inertia particles are thrown out of the mean flow by turbulent eddies embedded within the mean flow. The net effect is that the mean separation for finite-inertia particles levels off a bit, but continues to increase relative to the passive

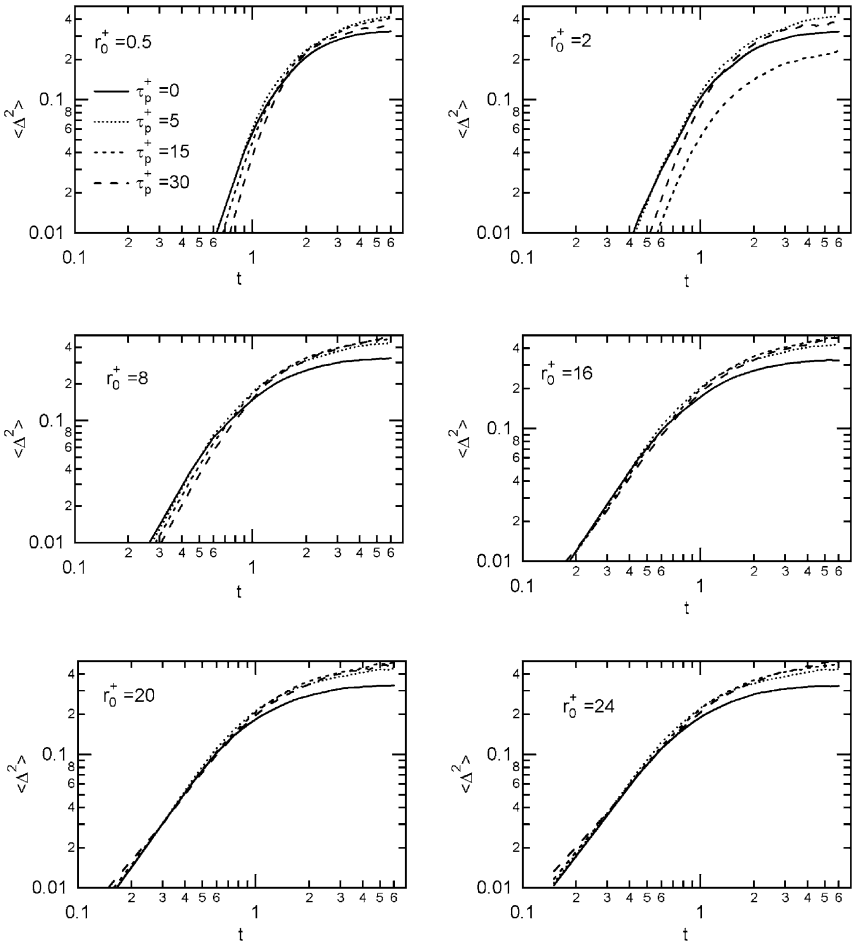

Fig. 13. Two-dimensional mean square separation of particle pairs in the *yz*-plane for $\tau_p^+ = 0, 5, 15$, and 30, and for six different initial separations.

tracer pairs. It is precisely this mechanism that transports higher inertia particles from the duct interior towards the duct wall, where they reside for a finite time period before either depositing or being carried back into the duct interior by the mean swirl, as visualized in Fig. 8.

5. Conclusions

Particle-laden turbulent flow through a straight square duct was studied using direct numerical simulation and Lagrangian particle tracking. To the best of our knowledge, this is the first study that uses direct numerical simulation coupled with Lagrangian particle tracking for a turbulent straight square duct flow. The directly simulated turbulent flow solution was validated using previously published DNS results for the same flow and Reynolds number.

The off-axis secondary flows unique to a square or rectangular duct tend to enhance lateral mixing by introducing an advective lateral transport in addition to the existing lateral turbulent dispersion of particles. Single-particle dispersion statistics indicate that low-inertia particles are more well-mixed throughout the cross-section of the duct and that high inertia particles tend to spread out more efficiently in the longitudinal direction, exhibiting a long tail behind the mean fluid flow. Pair dispersion statistics indicate that higher inertia particles are carried to the duct walls by the mean secondary flow, whereas passive tracers are more efficiently transported to the walls and back to the core in an oscillatory fashion.

Acknowledgement

We acknowledge the generous use of computational resources at the Texas A&M Supercomputing Facility. A small part of computations was performed on the National Science Foundation Terascale Computing System at the Pittsburgh Supercomputing Center using NSF-NPACI grant no. CTS030005P. Partial financial support from the Comprehensive Test Ban Treaty Organization (CTBTO) through the Lovelace Respiratory Research Institute under contract no. JK020160 is gratefully acknowledged. We also thank Professor C.S. Campbell for useful discussions concerning interpretation of the results and Dr. M.D. Deshpande for providing an earlier version of the flow simulation code.

References

Brooke, J.W., Hanratty, T.J., McLaughlin, J.B., 1994. Free-flight mixing and deposition of aerosols. Phys. Fluids 6, 3404–3415.

Elghobashi, S., Truesdell, G.C., 1992. Direct simulation of particle dispersion in a decaying isotropic turbulence. J. Fluid Mech. 242, 655–700.

Gavrilakis, S., 1992. Numerical simulation of low-Reynolds-number turbulent flow through a straight square duct. J. Fluid Mech. 244, 101–129.

La Porta, A., Voth, G.A., Crawford, A.M., Alexandar, J., Bodenschatz, E., 2001. Fluid particle accelerations in fully developed turbulence. Nature 409, 1017–1019.

MacInnes, J.M., Bracco, F.V., 1992. Stochastic particle dispersion modeling and the tracer-particle limit. Phys. Fluids A 4, 2809–2824.

Marchioli, C., Giusti, A., Salvetti, M.V., Soldati, A., 2003. Direct numerical simulation of particle wall transfer and deposition in upward turbulent pipe flow. Int. J. Multiphase Flow 29, 1017–1038.

Maxey, M.R., 1987. The motion of small spherical particles in a cellular flow field. Phys. Fluids 30, 1915–1928.

McLaughlin, J.B., 1989. Aerosol particle deposition in numerically simulated channel flow. Phys. Fluids A 1, 1211–1224.

Ott, S., Mann, J., 2000. An experimental investigation of the relative diffusion of particle pairs in three-dimensional turbulent flow. J. Fluid Mech. 422, 207–223.

Reeks, M.W., 1977. Dispersion of small particles suspended in an isotropic turbulent fluid. J. Fluid Mech. 83, 529–546.

Robinson, S.K., 1991. Coherent motions in the turbulent boundary layer. Annu. Rev. Fluid Mech. 23, 601–639.

Rovelstad, A.L., Handler, R.A., Bernard, P.S., 1994. The effect of interpolation errors on the Lagrangian analysis of simulated turbulent channel flow. J. Comput. Phys. 110, 190–195.

Saffman, P.G., 1965. The lift on a small sphere in a slow shear flow. J. Fluid Mech. 22, 385–400.

Squires, K.D., Eaton, J.K., 1991. Measurements of particle dispersion obtained from direct numerical simulations of isotropic turbulence. J. Fluid Mech. 226, 1–35.

Taylor, G.I., 1954. The dispersion of matter in turbulent flow through a pipe. Proc. R. Soc. London Ser. A 223, 446–468.

Uijttewaal, W.S.J., Oliemans, R.V.A., 1996. Particle dispersion and deposition in direct numerical and large eddy simulations of vertical pipe flows. Phys. Fluids 8, 2590–2604.

Vazquez, M.S., Metais, O., 2002. Large-eddy simulation of the turbulent flow though a heated square duct. J. Fluid Mech. 453, 201–238.

Virant, M., Dracos, T., 1997. 3D PTV and its application on Lagrangian motion. Meas. Sci. Technol. 8, 1539–1552.

Winkler, C.M., Rani, S.L., Vanka, S.P., 2004. Preferential concentration of particles in a fully developed turbulent square duct flow. Int. J. Multiphase Flow 30, 27–50.

Yeung, P.K., 2002. Lagrangian investigations of turbulence. Annu. Rev. Fluid Mech. 34, 115–142.

Yeung, P.K., Pope, S.B., 1989. Lagrangian statistics from direct numerical simulations of isotropic turbulence. J. Fluid Mech. 207, 531–586.